



A positioning algorithm for SPH ghost particles in smoothly curved geometries

Luis Vela Vela ^{*}, J.M. Reynolds-Barredo, Raul Sánchez

Departamento de Física, Universidad Carlos III, Leganés, Spain

HIGHLIGHTS

- An algorithm to place ghost particles across curved boundaries is developed.
- The algorithm is explicitly implemented in simple 3D geometries (cylinder, sphere, torus).
- The results converge to the usual mirror-technique when the curvature is negligible.
- The solutions were successfully tested in static and dynamical scenarios and their performance was characterised showing a clear improvement with respect to the usual method.

ARTICLE INFO

Article history:

Received 17 April 2018

Received in revised form 1 August 2018

Keywords:

SPH
Smoothed particle hydrodynamics
Ghost particles
Boundary conditions

ABSTRACT

An algorithm to place ghost particles across the domain boundary in the context of Smoothed Particle Hydrodynamics (SPH) is derived from basic principles, and constructed for several simple, three-dimensional, geometries. The performance of the algorithm is compared against the more commonly used “*mirrored with respect to the local tangent plane*” approach and shown to converge to it whenever the distance of the particles to the reflecting boundary is much smaller than a local measure of the surface’s curvature. The algorithm is demonstrated, tested and compared against the usual approach via simulations of a compressible flow around a cylinder, and the numerical cost of implementing it is addressed. We conclude that use of ghost particles to enforce boundary conditions is not only viable in the presence of smoothly curved boundaries, but more robust than the usual method for low-resolution scenarios.

© 2018 Elsevier B.V. All rights reserved.

1. Introduction

Smoothed Particle Hydrodynamics, or SPH for short, was introduced in the 70s by Gingold and Monaghan [1] together with Lucy [2] as a Lagrangian numerical method to solve the equations of Hydrodynamics [3]. Since its creation it has had great success in studying not only Hydrodynamical systems [4–6] but also in the context of Magnetohydrodynamics [7–10]. In SPH a number of particles are considered to serve as interpolation nodes where the value of any field of interest (density, velocity, etc.) can be easily found. This interpolation permits the discretisation of the spatial derivatives on a co-moving frame to obtain evolution equations for the particle’s position, velocity, mass density, internal energy and magnetic field. In contrast to what is done in other methods such as particle-in-cell where the electromagnetic fields are calculated over a well-structured grid, in SPH all the fields are “carried by the particles” and are evaluated via interpolation formulas.

^{*} Corresponding author.

E-mail address: luelav@fis.uc3m.es (L.V. Vela).

In spite of the relative success that SPH has had, it is yet not clear what is the most appropriate approach for handling the presence of boundaries. Astrophysical applications do not have to worry about this since most of these simulations take place in infinite (fully periodic) domains, but industrial applications of non-conducting fluids, or the study of laboratory plasmas do since hard boundaries and conducting walls are ubiquitous. One common approach to deal with the presence of boundaries is the use of ghost particles [11–15]. This approach was inspired by the ghost cells of finite-difference methods and it relies on the placing of *extra* particles on the outer side of the boundary with tailored properties of their fields so they mimic the effects of a solid boundary. The precise implementation of ghost particles changes widely across the literature, but here we will use the approach taken by Colagrossi [11] and by Monaghan [12] as our reference.

In their implementation the ghost particles are a reflection of the closest inner particles to the boundary with respect to the local tangent plane. The density, temperature and pressure fields of the ghost particle are then set to be equal to their inner counterpart, while the normal component of the velocity vector receives the opposite sign and the tangential component can remain the same (free-slip condition) or can also be reversed (no-slip condition). These authors show that this simple principle effectively enforces appropriate boundary conditions on the fluid in the presence of planar walls. The presence of curved boundaries however, must be handled with care since it is not a trivial matter. In his paper, Colagrossi [11] considers the case of a wall that is smoothly convex and shows that this causes an accumulation of mass, or ghost-mass to be precise, on the outside of the boundary due to the “lensing” effect that such wall has on the mirrored ghost particles. Colagrossi alerts of the dangers of this accumulation and states that a correction must be put in place although this correction is never specified.

In this paper we will try to contribute to the current understanding of how to use ghost particles in the vicinity of smoothly-curved surfaces in a manner consistent with the SPH equations. The present paper is organised as follows. First, we address in Section 2 the problem of using ghost particles with curved boundaries and identify the basic characteristics that any solution to the problem must have. In Section 3 we introduce the algorithm that will allow us to construct such solution for a restricted set of geometrical scenarios. In Section 4 we explicitly solve the problem for three common, three-dimensional, geometries. In Section 5 we show that our solutions converge to the typical one in the limiting case where the curvature of the surface is negligible. Section 6 addresses questions regarding the numerical costs of the new solutions. A static comparison of our solutions with the typical mirror map is done in Section 7 while Section 8 offers a dynamical example of compressible flow where our method outperforms the typical approach. Finally, the conclusions are given in Section 9.

2. The ghost particle approach

The implementation of ghost particles in SPH can be divided into two main steps: (I) For a given internal, or inner, particle i whose position is \mathbf{r}_i , one has to determine the precise position \mathbf{r}_i' of the ghost particle corresponding to it. (II) Once this has been done, one assigns to the ghost particle the same values of the fields as the inner particle (except the velocity field where the normal component ought to be reversed and the tangential component may or may not depend on the type of boundary condition required).

Applying this recipe to the density field, however, is a subtle matter. Consider again the inner particle \mathbf{r}_i . The value of the density field here ρ_i is given by:

$$\rho_i = \sum_{j \in \mathcal{N}_i} m_j W(|\mathbf{r}_i - \mathbf{r}_j|, H_i) \quad (1)$$

Here, the summation is carried over all the j -particles who happen to lie in the neighbourhood of i (that is, $j \in \mathcal{N}_i$), m_j are their masses, the function W is the usual SPH interpolation kernel (we use the 4th-order Wendland Kernel [16]) and H_i is the support radius of W .

One can clearly see from Eq. (1) that the value of the density field of the i th particle is a direct consequence of the relative distance to its neighbours and their respective masses. This is of categorical importance because if this particular arrangement of particles around i were not to be the same as the one around its ghost particle i' , then $\rho_{i'}$ would not coincide with the value of ρ_i and the density boundary condition would not be enforced properly. This can lead to a myriad of spurious results, some of which will be illustrated later.

One can advance by making the following approximation:

$$\rho_i \approx m_i \sum_{j \in \mathcal{N}_i} W(|\mathbf{r}_i - \mathbf{r}_j|, H_i) = m_i n_i \quad (2)$$

where n_i stands for the node density:

$$n_i = \sum_{j \in \mathcal{N}_i} W(|\mathbf{r}_i - \mathbf{r}_j|, H_i). \quad (3)$$

This approximation is valid whenever the value of the mass does not change very much across the neighbouring particles of i and becomes an equality when all the particles have the same mass. In this case, one can fiddle with either $m_{i'}$ or $n_{i'}$ in order to enforce $\rho_{i'} = \rho_i$.

At this point we find three different ways in which to enforce boundary conditions on the density field using ghost-particles:

- (A) Position the ghost particle so that it mirrors the position of the inner particle with respect to the local tangent plane and simply assign it equal values:

$$\rho_{i'} = \rho_i \tag{4}$$

- (B) Position the ghost particle so that it mirrors the position of the inner particle with respect to the local tangent plane. Then compute the local node-density using Eq. (3) and set the value of the mass of the ghost particle to achieve equal mass-density values:

$$\rho_{i'} = m_{i'} n_{i'} \tag{5}$$

where,

$$m_{i'} = \frac{\rho_i}{n_{i'}} \tag{6}$$

and $n_{i'}$ is computed via Eq. (3).

- (C) Keep the masses of the all particles in the simulation equal (inner and ghost alike) and construct a map $\mathbf{r}_{i'} = \Psi(\mathbf{r}_i)$ such that $n_{i'}$ equals n_i (with $n_{i'}$ given by Eq. (3))

In the presence of planar boundaries the map Ψ reduces to a simple reflection (this reflecting map or “mirror-map” will be denoted from now on as Ψ_0) and all previous approaches are equivalent. The presence of smoothly-curved boundaries however can, and will, distort the patterns of the particles as they are mapped onto their ghost counterparts. It is in these cases when the three ways presented here are no longer equivalent.

The first approach (A) is the “quick and dirty” solution to the problem. The density field does give the correct solution, that is $\rho_{i'} = \rho_i$, but it is not consistent with the SPH density estimate (Eq. (1)) in the ghost region.

Approach (B) seems to give the simplest correct answer at the expense of having to treat every particle with a different mass. This is not a heavy burden to carry when a code is being developed, but one has to be careful with this option. Method (B) relies on the approximation made in Eq. (2) which, as discussed before, might not always hold true. Also, there have been numerous studies pointing at the necessity of keeping the masses of the SPH particles equal to each other. Failing to do so often results in spurious numerical artefacts [17,18]. For this reason most modern implementations avoid this “different mass” approach for the inner particles.

One could, however, make the case that such cautionary measures need only apply to inner particles but not to ghost particles. This would tempt us to maintain constant mass among the inner particles and vary the masses of the ghost particles in accordance to option (B). This is however not a good idea since the energy of the system would not be conserved. To illustrate this, consider an internal particle heading towards the boundary at a right angle with mass m and velocity $\mathbf{v} = v_n \hat{\mathbf{n}}$ where $\hat{\mathbf{n}}$ is the outward pointing normal at the impact point. Ideally, one such particle should bounce off from the wall in an elastic manner, that is $v_n^{after} = -v_n^{before}$. However, if the effect of such wall is going to be replicated via a ghost particle of mass m' and velocity $-v_n$ then v_n^{after} for the inner particle will be:

$$v_n^{after} = v_n^{before} \left(1 - \frac{4}{1 + m/m'} \right) \tag{7}$$

This means that the effect of an elastic collision against the wall (that is $v_n^{after} = -v_n^{before}$) can *only* be replicated via ghost particles of mass m' such that $m' = m$. We discard option B altogether.

The third approach (C) is difficult to implement since it introduces the map Ψ for which there seems to be infinite freedom to choose it from. In this manuscript we will attempt to derive a differential equation for the map Ψ that will allow us to solve it analytically for simple geometries like cylinders (or 2D circles), spheres and tori. We will also prove that all the solutions resemble the mirror map Ψ_0 in the limiting case when \mathbf{r}_i lies very close to the boundary such that the effects of the wall-curvature can be neglected.

3. Outline of the problem, and sketch of a solution

We begin by considering a flat surface. Every particle inside the boundary will be mirrored to the other side of the boundary in a rather uneventful way. If the particle is at position $\{x, y, z\}$ with $z > 0$, and the boundary in question is the plane $z = 0$, then its ghost particle will be placed at $\{x, y, -z\}$. Every particle close to the surface will undergo this map and due to the flatness of the boundary *the relative positions of the ghost particles will mimic the relative positions of their corresponding inner counterparts*. This is indeed fortunate because, if we have used Eq. (1) to compute the density of the inner particles, then there is no need to do it again for the ghost particle. We simply have to copy/paste the values of the density field inside to the outside particles.

However, in the event of a surface which is not exactly flat, a simple map like this will in fact distort the relative positions of the ghost particles (as in Colagrossi’s case [11] where the convex wall created a lensing effect and an excess of ghost mass across the boundary), and the density estimate will not give the same value when evaluated over the ghost particle since all its neighbours are in a slightly different configuration (see Fig. 1). As illustrated in Fig. 2, this distortion has nothing to do with the “border effect” that particles feel when they happen to be at the border of a particle cloud and all their neighbours are disproportionally distributed to one side of its vicinity.

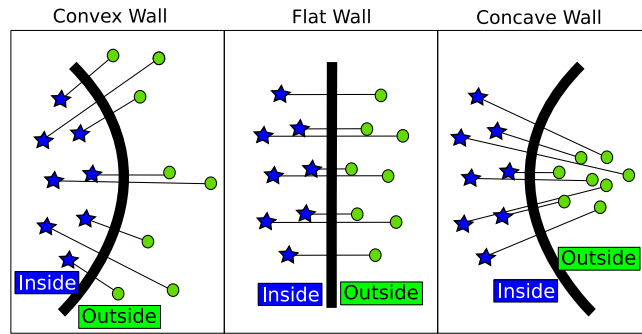


Fig. 1. Illustration of the spurious “lensing” effect created whenever the “reflect with respect to the local tangent plane”-principle is used in the presence of curved walls. Flat walls do not disturb the relative positions of the particles and therefore the particle density remains the same in both the inside and the outside. Concave and convex walls however, create an accumulation/dispersion of particles which affect the SPH estimation of the density field in the ghost region.

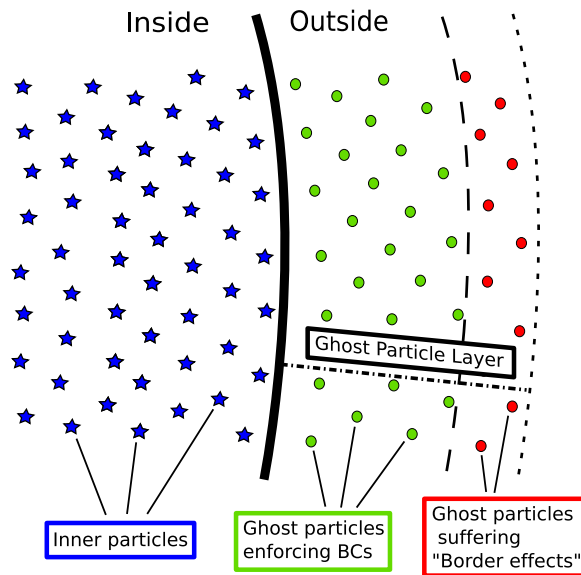


Fig. 2. Three distinct regions are identified in the vicinity of the boundary of an SPH simulation: (1) The inside is populated by regular particles. (2) Adjacent to it we have ghost particles which have suffered a deformation in their relative positions due to the map Ψ but do not suffer border effects. (3) At the very end we have particles where the border effect is dominant.

When constructing the map Ψ in the non-planar case, we must ensure that the density estimate, when evaluated on the ghost particle, gives the same result as the inner particle. That is, $\rho_{i'} = \rho_i$. Now, given that m is the same over all the particles (ghost and inner), the mapping has to be such that the node-density remains constant: $n_{i'} = n_i$. To construct such a map, we reason as follows: Consider a particle whose position is given by $\mathbf{r}_i = \{x_i, y_i, z_i\}$, while the ghost particle will be placed at $\mathbf{r}_{i'} = \{x'_i, y'_i, z'_i\}$. The mapping Ψ will then be given, in general, by the functions ψ_x, ψ_y and ψ_z :

$$\begin{Bmatrix} x'_i \\ y'_i \\ z'_i \end{Bmatrix} = \begin{Bmatrix} \psi_x(x_i, y_i, z_i) \\ \psi_y(x_i, y_i, z_i) \\ \psi_z(x_i, y_i, z_i) \end{Bmatrix} \tag{8}$$

The geometry of the problem must now be considered. In particular, we will assume possible to switch from our coordinates $\{x, y, z\}$ to a set of coordinates $\{s, u, v\}$ such that:

- The boundary can be approximated by the surface $s = 0$, with $s < 0$ for the inside volume, and $s > 0$ for the outside.
- The shortest line joining \mathbf{r}_i with the boundary surface can be approximated by the intersection of the surfaces $v = C_v$ and $u = C_u$ with C_v and C_u appropriate constants.

In this set of coordinates we can restrict the map Ψ to only affect the s -coordinate while leaving both u and v untouched. This fact guarantees the absence of tangential components in the interaction between inner and ghost particles.

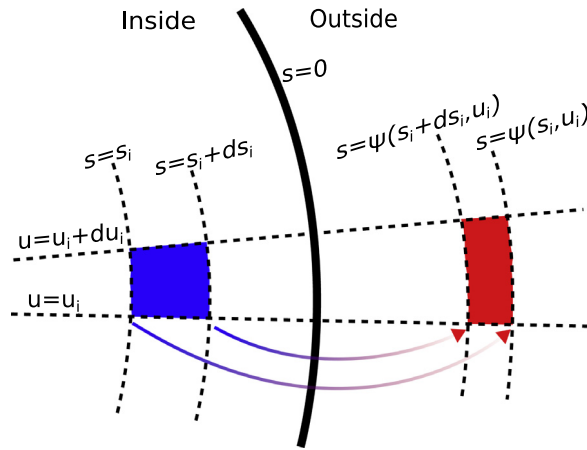


Fig. 3. Two-Dimensional illustration of how the continuum-limit expression in Eq. (11) must be understood. The map ψ is such that the blue region, when mapped across the boundary into the red region, is deformed but maintains the same area. Thus guaranteeing that the node density field will remain invariant under ψ .

Locally, the set of coordinate $\{s, u, v\}$ can always be chosen to be flat, that is Euclidean with unit Jacobian, however the idea behind the algorithm here is to go beyond this and chose the next best system of coordinates that fulfils conditions 1 and 2, we will see examples of how this can be done in the following sections. In the $\{s, u, v\}$ coordinates the mapping becomes:

$$\begin{Bmatrix} s'_i \\ u'_i \\ v'_i \end{Bmatrix} = \begin{Bmatrix} \psi(s_i, u_i, v_i) \\ u_i \\ v_i \end{Bmatrix} \tag{9}$$

The fact that node-density estimate must remain constant along such map can be expressed, in terms of the SPH density estimator, as:

$$\sum_{j \in \mathcal{N}_i} W_{ij}(H_i) = \sum_{k \in \mathcal{N}'_i} W_{ki'}(H'_i). \tag{10}$$

To find the constraints imposed on the function ψ by this condition, we proceed to take the continuum limit, in the SPH sense, of Eq. (10). This can be done by letting $H \mapsto 0$ while ensuring $N_{nei} \mapsto \infty$, where N_{nei} is the number of interacting neighbours of each particle. This leads to:

$$\begin{aligned} & \int_{v_i}^{v_i+\Delta v_i} \int_{u_i}^{u_i+\Delta u_i} \int_{s_i}^{s_i+\Delta s_i} n(s_i, u_i, v_i) \mathcal{J}(s_i, u_i, v_i) ds du dv = \\ & = \int_{v_i}^{v_i+\Delta v_i} \int_{u_i}^{u_i+\Delta u_i} \int_{\psi(s_i+\Delta s_i, u_i, v_i)}^{\psi(s_i, u_i, v_i)} n(\psi(s_i, u_i, v_i), u_i, v_i) \mathcal{J}(\psi(s_i, u_i, v_i), u_i, v_i) ds du dv \end{aligned} \tag{11}$$

where the node density is integrated over a small region around the points \mathbf{r}_i and \mathbf{r}'_i taking into account the Jacobian of the coordinate system \mathcal{J} .

To understand better the meaning of Eq. (11) we refer the reader to Fig. 3 where a 2D version of the problem is illustrated. In it, it is shown how the blue region, that is, a small region around point $\{s_i, u_i\}$, is being mapped into the red region around $\{s'_i, u'_i\}$. It is important to notice that the map ψ will necessarily distort the shape of the regions (due to the curvature of the boundary) in order to keep the areas of the two regions constant.

It is also worth noting that the limits of the integrals on the right hand side of Eq. (11) seem to have been inverted. This is a consequence of the fact that, at the boundary, we must have:

$$\psi(0) = 0 \quad \text{or} \quad \Psi(\mathbf{r}_i) = \mathbf{r}_i \tag{12}$$

That is, points that are closer to the boundary will be mapped to positions that are close to the boundary, while points that are far away will be mapped into far away positions (see Fig. 3). Dropping the integrals over u and v and taking the limit $\Delta s \mapsto 0$ one can write:

$$\frac{\partial \psi(s, u, v)}{\partial s} = - \frac{\mathcal{J}(s, u, v)}{\mathcal{J}(\psi(s, u, v), u, v)} \tag{13}$$

The function ψ , and consequentially the map Ψ , can be obtained by solving Eq. (13), with the boundary conditions given by Eq. (12).

4. Some explicit solutions

4.1. A flat surface

Eq. (13) can be easily evaluated near a flat surface. In this case the Jacobian is the same at both sides of the boundary and the ODE transforms into:

$$\frac{\partial \psi(s, u, v)}{\partial s} = -1 \tag{14}$$

Upon integration and taking into account the boundary conditions in Eq. (12), one finds the solution:

$$\psi(s, u, v) = -s \tag{15}$$

In this particular case the map $\psi(s, u, v)$ is only a function of s since the curvature is constant along the surface. This means, an inner particle a distance d from the surface (that is $s = -d$) will have its corresponding ghost particle at a distance d on the other side of the boundary. For the flat surface one concludes:

$$\Psi = \Psi_0 = -s \tag{16}$$

It is worth noting that since any curved surface resembles a flat plane when looked upon sufficiently close, all solutions of Eq. (13) should necessarily look like a mirror-map when sufficiently near to the surface, that is, for values of the coordinate s that are close to zero. Next, we will explore some curved geometries that are of interest and that can be solved analytically.

4.2. Cylinder

For the case of the cylinder of radius R one can choose our $\{s, u, v\}$ coordinates in terms of cylindrical coordinates $\{r, \theta, z\}$:

$$r = R + s \quad \theta = u \quad z = v \tag{17}$$

The Jacobian is then given by $\mathcal{J} = r$ and the differential equation that defines the map is:

$$\frac{\partial \psi(s, u, v)}{\partial s} = -\frac{R + s}{R + \psi(s, u, v)} \tag{18}$$

The solution can be found by straightforward integration after taking into account the boundary conditions given by Eqs. (12). The final result can be written implicitly using the function $g(x)$:

$$g(R + \psi) + g(R + s) = 2g(R) \tag{19}$$

where $g(x) = x^2$. The explicit shape of ψ can be found by inverting the function $g(x)$:

$$\psi = g^{-1}\left(2g(R) - g(R + s)\right) - R \tag{20}$$

This can be explicitly written as:

$$\psi(s, u, v) = \sqrt{2R^2 - (R + s)^2} - R \tag{21}$$

As expected, the map does not depend on the angular coordinate u , nor on the longitudinal coordinate v . Also, notice how this solution is applicable to two dimensional circular domains as well.

4.3. Sphere

In the case of the sphere of radius R a similar procedure is followed. The coordinates to be used are:

$$r = R + s \quad \theta = u \quad \phi = v \tag{22}$$

where $\{r, \theta, \phi\}$ are the usual spherical coordinates. The Jacobian is given by $\mathcal{J} = r^2 \sin \phi$ and the differential equation that defines the map becomes:

$$\frac{\partial \psi(s, u, v)}{\partial s} = -\frac{(R + s)^2}{(R + \psi(s, u, v))^2} \tag{23}$$

Its solution can be written as:

$$\psi = g^{-1}\left(2g(R) - g(R + s)\right) - R \tag{24}$$

although this time $g(x) = x^3$. The expression for ψ then becomes:

$$\psi(s, u, v) = \sqrt[3]{2R^3 - (R + s)^3} - R \tag{25}$$

that is again independent of u and v .

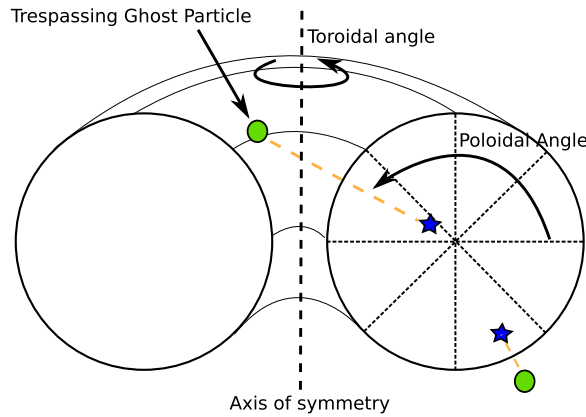


Fig. 4. The case of a torus with circular cross section and aspect ratio $R/a < 2$. We can see how particles with poloidal coordinate $\theta \approx \pi$ can get mapped beyond the axis of symmetry of the torus. At this point they will interact with the inner particles on the opposite part of the domain introducing spurious forces on the system.

4.4. Torus

The last example that will be examined is a torus of circular cross section and aspect ratio R/a . The coordinates $\{s, u, v\}$ in terms of the toroidal coordinates $\{r, \theta, \phi\}$, are:

$$r = a + s \quad \theta = u \quad \phi = v \tag{26}$$

with a Jacobian $\mathcal{J} = r(R + r \cos \theta)$. The resulting differential equation for Ψ is:

$$\frac{\partial \psi(s, u, v)}{\partial s} = -\frac{(s + a)(1 + (s + a)B_u)}{(\psi + a)(1 + (\psi + a)B_u)} \tag{27}$$

where the parameter $B_u = \cos(u)/R$ contains the dependency on the poloidal angle. The analytical solution, again, can be expressed as:

$$\psi = g^{-1} \left(2g(a) - g(a + s) \right) - a \tag{28}$$

with:

$$g(x) = B_u \frac{x^3}{3} + \frac{x^2}{2} \tag{29}$$

Interestingly, an angular dependency appears in the solution for the torus. This is a consequence of the different curvature values that exist along the surface of the torus. It also means that our map ψ will behave differently for different poloidal angles. Also notice how the function $g(x)$, now a third degree polynomial, is not so easily inverted (see the [Appendix](#) for details).

4.5. Special considerations regarding the toroidal geometry

As mentioned before, the resulting map has a poloidal dependence implying that ghost particles with different poloidal angle will be placed in different ways. It can be proven (see [Appendix](#) for details) that the toroidal map at points with coordinate $u = \theta = \pm\pi/2$ is exactly the cylindrical-map, and this result is independent of the torus' aspect ratio.

Another interesting behaviour appears for a torus with aspect ratio equal to 2 at points with coordinates $u = \theta = \pm\pi$, that is, for points close to the inner hole of the torus. For these points the map ψ becomes identical to the mirror map. This behaviour can also be seen graphically in [Fig. 5](#), where the torus branch $\theta = \pi$ will drift towards the mirror map as the aspect ratio approaches two.

When the aspect ratio becomes smaller than two, the toroidal branch drifts past the mirror map and the ghost particles will be positioned beyond the axis of symmetry of the torus. This situation (illustrated in [Fig. 4](#)) is completely undesirable and should be avoided at all costs. Therefore, the use of ghost particles must be handled with care when dealing with toroidal geometries whose aspect ratio is smaller than two. This could be achieved, for instance, by increasing the number of particles sufficiently as to make the thickness of the ghost layer thin enough so this trespassing never takes place.

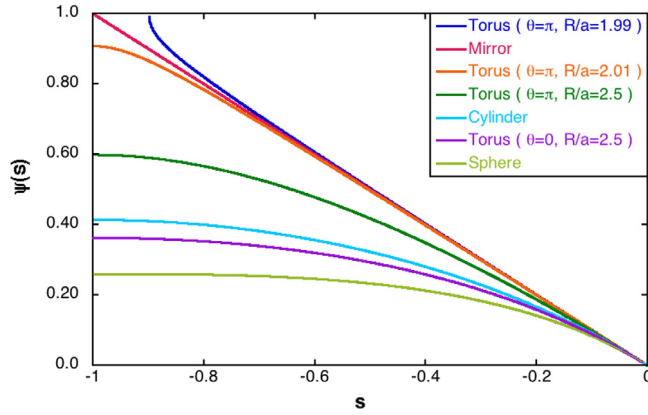


Fig. 5. The analytical solution of ψ is shown for the simple geometries of a cylinder, a sphere and a torus of circular cross section and aspect ratio $R/a = 2.5$ (for the poloidal positions $\theta = 0$ and $\theta = \pi$). The solutions are all compared against the mirror-map to which, as expected, all converge towards the mirror map near the boundary ($s = 0$). Also the toroidal maps for $\theta = \pi$ and $R/a = 2.00 \pm 0.01$ have been included to demonstrate the behaviour of ψ in tori with aspect ratio smaller than two.

5. Behaviour near the surface

While deriving the previous solutions, the function $g(x)$ was introduced. This function is convenient because it makes it easy to prove that the three explicit solutions converge to the mirror-like behaviour near the domain boundary $s = 0$. We begin by noticing that all three solutions have the same canonical form:

$$g(R + \psi) + g(R + s) = 2g(R) \tag{30}$$

Near the surface the following approximations can be made:

$$g(R + \psi) = 2g(R) - g(R + s) \tag{31}$$

$$g(R + \psi) = g(R) - s \left(\frac{g(R + s) - g(R)}{s} \right) \tag{32}$$

$$g(R + \psi) \approx g(R) - sg'(R) \tag{33}$$

$$g(R + \psi) \approx g(R - s) \tag{34}$$

$$\psi \approx -s \tag{35}$$

where, in the case of the torus, the quantity R must be replaced by its minor radius a . This proves that all the previous examples behave like a mirror near the surface. This is better illustrated in Fig. 5 where the three solutions (Cylinder, Sphere and Torus) are plot together with the mirror-map solution. We see how close to $s = 0$ they all converge to ψ_0 . It is also noticeable how the two branches of the torus ($\theta = 0$ and $\theta = \pm\pi$) are always below and above the cylinder solution respectively. This remains true even in the event of $R/a \mapsto \infty$ where each branch converges to the cylinder solution, as one would expect.

6. Numerical cost of the non-linear solutions

The maps found so far imply that ghost particles will be positioned in a slightly more complicated manner: Instead of calculating the ghost particle position through the linear map $\psi_0 = -s$, we will need to evaluate the corresponding non-linear Ψ functions given in Eqs. (21), (25) and (28). In this section we address the question of the numerical cost of such evaluation in the geometries considered here.

We will place $N = 10^6$ particles inside (i) A sphere of radius $r = 1$, (ii) A cylinder or radius $r = 1$ and length $L_z = 2\pi$, and (iii) A torus of minor radius $a = 1$ and outer ratio $R = 3$. In each case, we will place the inner particles in a random initial position, and compute the time needed to place all the ghost particles. The results are displayed in Table 1.

We see how the increase in CPU time is directly proportional to the complexity of the function $g(s)$ and its inverse $g^{-1}(s)$: The spherical and cylindrical cases notice an increase of about 1% in CPU time, while the toroidal case, where the $g^{-1}(s)$ is detailed in the Appendix, suffers an increase of about 10%. The implementation of the toroidal function $g^{-1}(s)$ has been done in the straightforward manner sketched in the Appendix where no optimisation has been considered. Finally, notice how this is not a CPU increment of the total time-step but only on the fraction corresponding to the ghost-particle positioning.

Table 1

Percentage of increased CPU time in positioning the ghost particles when using the non-linear solution with respect to the time needed while using the linear map ψ_0 . It can be seen that in the cylindrical and spherical cases the use of the non-linear map means a 1% increase in the CPU time required to do the positioning, while in the toroidal case, where the complexity of the $g(s)$ function increases, the CPU time increase is of about 10%. The error bars have been calculated as the standard deviation of a set of 10 different measurements, each coming from a different random initial configuration.

3D Geometry	CPU time increment [%]
Cylinder	0.63 ± 0.02
Sphere	1.36 ± 0.03
Torus	10.3 ± 0.3

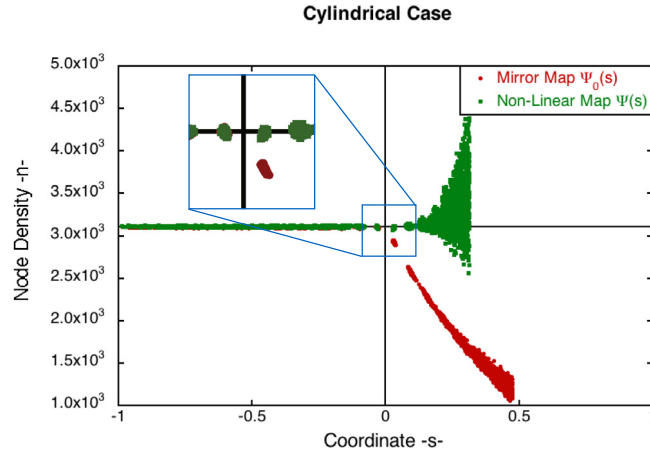


Fig. 6. Resulting node density field both inside and outside of the boundary for the cylinder. The constant inside values were constructed with ALARIC, while the outer values were calculated using Eq. (3) after the ghost particle positions were determined using both ψ_0 and ψ for the cylindrical case. The results offered by ψ remain constant around the desired value while the ones offered by ψ_0 rapidly decay (see zoomed-in region).

7. Static test of the solutions

7.1. Cylinder

To show the performance of the map found for the cylindrical case, we have initialised 50K particles inside a periodic cylinder of unit radius which extends from $z_{min} = -3$ to $z_{max} = +3$. The particles have been positioned following the ALARIC algorithm [18] to give rise to a flat density profile, that is $\rho = \text{constant}$. All the particles in this scenario have the same mass which, in turn, guarantees that the node-density field will also be constant $n = \text{constant}$. We then proceeded to place the ghost particles across the boundary using the usual mirror map ψ_0 and the newly constructed map ψ . 50K ghost particles were used to guarantee that every internal particle has a ghost counterpart.

Fig. 6 shows the resulting node-density estimate (computed from Eq. (3)) for all the ghost particles across the boundary. The figure clearly illustrates the ability of the map ψ to maintain the node density field constant outside of the domain boundary. It also shows how the mirror map ψ_0 creates a rapidly decaying field outside of the boundary as shown in the small zoomed-in rectangle inside Fig. 6.

It is also visible in the graph that, while the values of the map ψ are indeed the correct ones at first, the values start to diverge once one goes away from the domain boundary. This variation can be attributed to (a) The distortions that are created by the map ψ in the “angular” variables u and v and (b) To the accumulation of particles at the outer most positions of the map. The first cause, as mentioned in the earlier sections, is related to the fact that the map ψ was forced to act only on the coordinate s while leaving u and v untouched. This allowed us to simplify the constraints on ψ and come up with an equation for it, namely Eq. (13). The consequence of this choice is illustrated in Fig. 3 where, in order to maintain the areas of the two regions equal, the mapped region becomes an elongated/contracted version of the original region. The related distortion in u and v however never affects the SPH kernel, which remains perfectly spherical. As a result of this asymmetry, noise appears in the resulting values of the node density field.

The second cause is the accumulation of ghost particles at the outermost radial positions. This can be seen in Fig. 5 where the cylindrical solution becomes almost flat around $s \approx -1$. This causes inner particles near the axis of the cylinder to be mapped to ghost particles with similar radial positions explaining the divergent values on the node density field shown in Fig. 6.

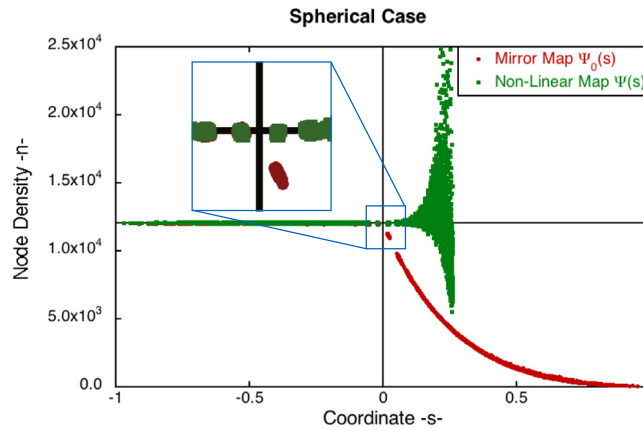


Fig. 7. Resulting node density field both inside and outside the boundary for the sphere. The outer values were calculated using Eq. (3) after the ghost particle positions were determined using both ψ_0 and ψ for the spherical case. The results offered by ψ remain constant around the desired value while the ones offered by ψ_0 not only rapidly decay but introduce small errors on the internal particles (see zoomed-in region).

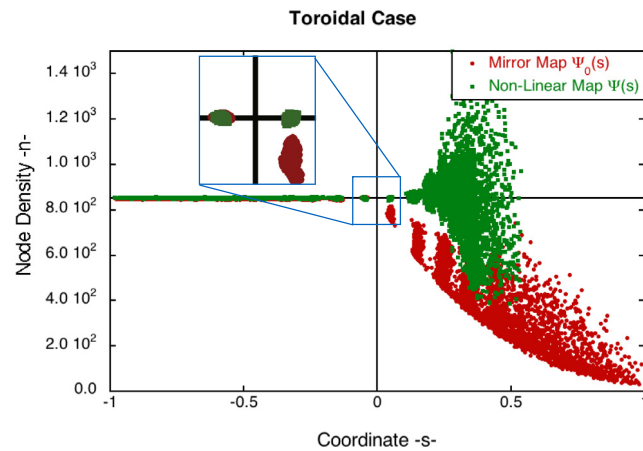


Fig. 8. Resulting node density field both before and after the boundary for the toroidal case. The behaviour of ψ is very similar to the spherical and cylindrical cases with one visible difference: the values of the density field have broadened horizontally due to the poloidal dependence of the surface curvature's.

7.2. Sphere

In the spherical case we have also used 50K internal and 50K ghost particles. The positions of the internal particles have been relaxed using ALARIC to reach a constant density value. Apart from the change in geometry, the spherical case is very similar to the cylindrical one (see Fig. 7). The node density field calculated on ghost particles mapped with ψ_0 decays rapidly while our solution delivers correct values near the boundary. A divergent behaviour of the node density field values for outer radial positions is also present much like in the cylindrical case, and because of the same reasons.

7.3. Torus (aspect ratio $R/a = 3$)

The same conditions are used to examine the toroidal case: 50K internal particles in a flat density configuration with 50K ghost particles outside. The results obtained for the torus, shown in Fig. 8, offer one new feature: the values of the node density field (for both ψ_0 and ψ) have been broadened horizontally. This is a direct consequence of the poloidal dependence of the surface curvature (captured by the parameter B_{II}). Notice how in this case as well, our solution delivers values of the node density field that properly enforce the required boundary conditions.

8. Dynamic test of the solutions

As a dynamical test, we consider the flow of a compressible liquid in a lattice of cylindrical obstacles. In our test, we consider the two-dimensional periodic computational domain $\{x, y\} \in [-0.5, 0.5] \times [-0.5, 0.5]$ with a circular obstacle of

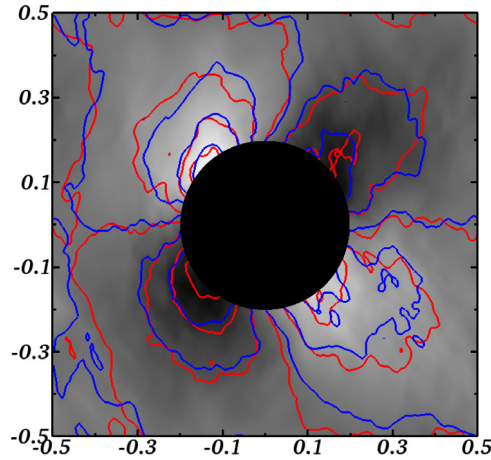


Fig. 9. Contour plots of the v_y field for the compressible flow around a circular obstacle where a free-slip condition on the velocity field has been enforced. The background heat map depicts the solution using the usual mirror-map. The red lines are contour lines around the values $\{0, \pm 1/12, \pm 1/6, \pm 1/4\}$. The blue contour lines correspond to the solution found with the non-linear map from Eq. (21). In spite of the noise, it is clear that both methods arrive at the same stationary solution.

radius $r = 0.2$ at the origin. The evolution equation for the velocity field has been modified to include a driving term of the form:

$$\frac{d\mathbf{v}_a}{dt} = \frac{v_0 - v_x}{\tau} \hat{\mathbf{x}} \tag{36}$$

which¹ effectively creates a constant flow in the x -direction with velocity v_0 . We run the simulation using both the usual mirror-map and the non-linear map from Eq. (21) to position the ghost particles and simulate the effect of a circular obstacle. The results are presented in the following subsections.

8.1. Medium-to-high resolution regime

We began by running the simulation with 10K particles for 10 s with $v_0 = 0.5$ and a free-slip boundary condition around the object. The results, shown in Fig. 9, show that there is no appreciable difference between using the mirror-map and the non-linear map.

In fact, as the resolution of the system is increased and the inter-particle spacing decreases, the ghost particle layer needed to enforce proper boundary conditions inside the circular object will become thinner and thinner. This means that the map Ψ will be evaluated at very small values of the radial coordinate s , and given that Ψ converges to Ψ_0 for small values of s , similar results are to be expected for well-resolved scenarios.

8.2. Low resolution regime

The benefits of the non-linear map is better observed when the resolution of the system is decreased and the agreement between Ψ and Ψ_0 is no longer guaranteed. To illustrate this, we have decreased the number of particles down to $N = 100$ and run the same simulation with different values of the reference velocity $v_0 \in \{0.05, 0.10, \dots, 0.75\}$ until $t = 10$. For each value of v_0 we run 20 simulations with a different random initialisation, and kept track of the maximum simulation time t_{\max} defined as:

$$t_{\max} = \min\{t_{\text{final}}, t_{\text{penetration}}, t_{\text{accumulation}}\} \tag{37}$$

where t_{final} is 10 s, $t_{\text{penetration}}$ marks the instant when a particle penetrates the circular obstacle for the first time and $t_{\text{accumulation}}$ marks the moment when an unusually high accumulation of ghost particles near the origin $\{0, 0\}$ shrinks their support radius H close to zero causing numerical instabilities.

Fig. 10 shows the mean value of t_{\max} as a function of the driving velocity v_0 . We can clearly see from the trends how the use of the linear map results in particle penetration or spurious mass-accumulation at the origin that can potentially terminate the simulation and crash it. On the other hand, the graph also shows how the runs where the non-linear map was used almost always reach the desired 10s of simulated time without any mishap.

¹ We will use $\tau = 1.0$ for all our simulations.

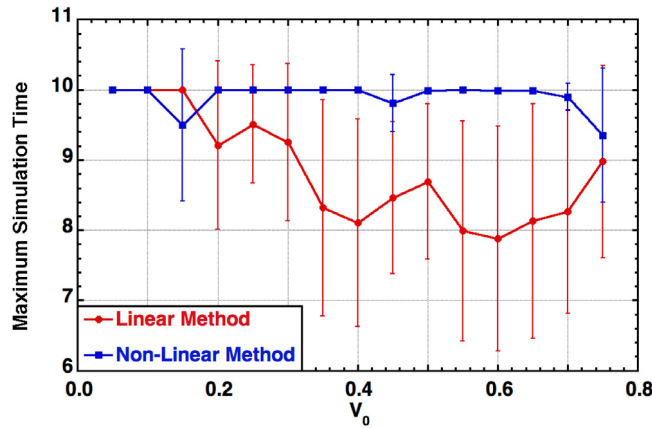


Fig. 10. Maximum Simulated time as a function of the driving velocity v_0 . We see how the simulations run with the mirror-map suffer from mishaps that quite often impedes the simulation to complete its simulation time without any mishaps. The blue line however, shows how the number, and frequency, of this mishap is reduced whenever the non-linear solution is used.

This result is very important since, in general, where flows are compressible and density can vary notoriously in space, any smoothly curved wall that is left with few particles around, and therefore is poorly resolved, our method guarantees a proper functioning of the SPH engine by avoiding particle penetration and mass accumulation around the centre of curvature of the surface. Using the non-linear method allows the simulation to deliver correct results, and more importantly not to crash, in low-resolution regimes.

9. Conclusions

The subtleties of the ghost particle approach to enforce appropriate boundary conditions on the density field around smoothly curved surfaces have been explored within the SPH framework.

We have formulated the problem in terms of the node-density field and have shown that a map ψ that places the ghost particles in such an arrangement so as to maintain the node-density constant can be constructed.

A differential equation to find such map, supplemented with appropriate boundary conditions, has been derived and constitutes the main result of this study. The differential equation has been solved for simple three dimensional geometries and these resulting maps have been tested in static and dynamic scenarios.

The static tests proved that adequate values of the node density field in the region next to the domain surface were obtained. Far away from the surface however, our solutions displayed a divergent behaviour which was explained in terms of the limitations imposed on the map ψ . This region with divergent values of the field can be avoided as long as the ghost boundary layer is thin enough so as to guarantee that the furthest mapped ghost particle does not enter such region.

The dynamical test with compressible flow around a lattice of cylindrical obstacles showed that for medium-to-high resolution regimes there is no visible difference between simulations that use the mirror-map and simulations that used the non-linear map. This is no surprise since the non-linear map ψ converges to ψ_0 for small values of the s -coordinate (as shown in Section 5) and the values of s are proportional to the inter particle spacing which decreases with the number of particles N . In the low resolution regime however, the difference is striking. Simulations run with the mirror-map were prone to particle penetration and numerical instabilities related to particle accumulation near the origin while the simulations run with the non-linear map almost always end the simulation without any mishap.

We believe that the proposed method, and the solutions found with it, allow the successful simulation of scenarios with smoothly curved boundaries using SPH-methods in a consistent manner, thus opening up the range of problems where it might be applicable.

Acknowledgements

This research was sponsored in part by the DGICYT (Dirección General de Investigaciones Científicas y Tecnológicas) of Spain under National Project No. ENE2015-68265. Research was also funded in part by the Erasmus Mundus Program: International Doctoral College in Fusion Science and Engineering FUSION-DC, Spain.

Appendix A. Explicit shape of the toroidal map

The explicit shape for the toroidal map is given by:

$$\psi = g^{-1}(2g(a) - g(a + s)) - a \tag{38}$$

where the function $g(x)$ is given by:

$$g(x) = B_u \frac{x^3}{3} + \frac{x^2}{2} \quad (39)$$

and,

$$B_u = \frac{\cos(u)}{R} \quad (40)$$

The inverse of $g(x)$ can then be expressed in terms of several intermediate definitions. In particular, the complex number z :

$$z = -\frac{1 + i\sqrt{3}}{2}, \quad (41)$$

the function $p(x)$,

$$p(x) = 12xB_u^2 - 1, \quad (42)$$

the function $\Delta(x)$

$$\Delta(x) = \sqrt[3]{p(x) + \sqrt{p^2(x) - 1}} \quad (43)$$

and the three branches:

$$g_0^{-1}(x) = \sqrt{2x} \quad (44)$$

$$g_+^{-1}(x) = \frac{1}{2B_u} \left(\frac{1}{\Delta(x)} + \Delta(x) - 1 \right) \quad (45)$$

$$g_-^{-1}(x) = \frac{1}{2B_u} \left(\frac{\bar{z}}{\Delta(x)} + z\Delta(x) - 1 \right) \quad (46)$$

With all this in hand, one can express g^{-1} as:

$$g^{-1}(x) = \begin{cases} g_+^{-1}(x) & B_u > 0 \\ g_0^{-1}(x) & B_u = 0 \\ \Re[g_-^{-1}(x)] & B_u < 0 \end{cases} \quad (47)$$

where \Re stands for the real part of the function.

Appendix B. Certain proofs for the toroidal map

The canonical form of the toroidal map is:

$$g(a + \psi) + g(a + s) = 2g(a) \quad (48)$$

This can be re-written as:

$$\left[(1 + \psi)^2 + (1 + s)^2 - 2 \right] - \mathcal{D} \left[(1 + \psi)^3 + (1 + s)^3 - 2 \right] = 0 \quad (49)$$

where,

$$\mathcal{D} = \frac{2a}{3R} \cos(u) \quad (50)$$

and both quantities, ψ and s , have been normalised to a . The expression can be grouped as follows:

$$(2 + 3\mathcal{D})(\psi + s) + (1 + 3\mathcal{D})(\psi^2 + s^2) + \mathcal{D}(\psi^3 + s^3) = 0 \quad (51)$$

The first interesting case comes from letting $\mathcal{D} = 0$ (which is equivalent to setting $u = \theta = \pm\pi/2$, or by letting $R/a \mapsto \infty$). For this choice one can easily obtain:

$$(\psi + 1)^2 + (s + 1)^2 - 2 = 0 \quad (52)$$

which is the same expression as the one used for the cylinder. This means the torus behaves like a cylinder in the limit of infinite aspect ratio, as one should expect, but also for points whose coordinates are $u = \pm\pi/2$. This second statement was already visible in the singular shape of $g_0^{-1}(r)$ which was to be used at those points exactly.

The next interesting case is $\mathcal{D} = -1/3$ for which we find:

$$\psi^3 + s^3 = 3(\psi + s) \quad (53)$$

The only viable solution is given by:

$$\psi = -s \quad (54)$$

that is, a mirror map. The case $\mathcal{D} = 1/3$ corresponds to points with coordinate $u = \pm\pi$ and a toroidal geometry with aspect ratio $R/a = 2$, the importance of this result is discussed in Section 4.5.

The last case, $\mathcal{D} = -2/3$, does not seem to give any new, nor relevant, information about the behaviour of the toroidal map for different poloidal angles.

References

- [1] R.A. Gingold, J.J. Monaghan, Smoothed particle hydrodynamics: theory and application to non-spherical stars, *Mon. Not. R. Astron. Soc.* 181 (3) (1977) 375–389.
- [2] L.B. Lucy, A numerical approach to the testing of the fission hypothesis, *Astron. J.* 82 (1977) 1013–1024.
- [3] D.J. Price, Smoothed particle hydrodynamics and magnetohydrodynamics, *J. Comput. Phys.* 231 (3) (2012) 759–794.
- [4] J.J. Monaghan, Smoothed particle hydrodynamics, *Annu. Rev. Astron. Astrophys.* 30 (1992) 543–574.
- [5] S. Li, W.K. Liu, Meshfree and particle methods and their applications, *Appl. Mech. Rev.* 55 (1) (2002) 1–34.
- [6] J.J. Monaghan, Smoothed particle hydrodynamics, *Rep. Prog. Phys.* 68 (8) (2005) 1703.
- [7] S. Rosswog, Astrophysical smooth particle hydrodynamics, *New Astron. Rev.* 53 (4) (2009) 78–104.
- [8] F.A. Stasyszyn, D. Elstner, A vector potential implementation for smoothed particle magnetohydrodynamics, *J. Comput. Phys.* 282 (2015) 148–156.
- [9] D.J. Price, J. Wurster, C. Nixon, T.S. Tricco, S. Toupin, A. Pettitt, C. Chan, G. Laibe, S. Glover, C. Dobbs, et al., Phantom: a smoothed particle hydrodynamics and magnetohydrodynamics code for astrophysics, 2017, arXiv preprint arXiv:1702.03930.
- [10] S. Vanaverbeke, R. Keppens, S. Poedts, H. Boffin, Gradsph: a parallel smoothed particle hydrodynamics code for self-gravitating astrophysical fluid dynamics, *Comput. Phys. Commun.* 180 (7) (2009) 1164–1182.
- [11] A. Colagrossi, M. Landrini, Numerical simulation of interfacial flows by smoothed particle hydrodynamics, *J. Comput. Phys.* 191 (2) (2003) 448–475.
- [12] J.J. Monaghan, J.B. Kajtar, SPH particle boundary forces for arbitrary boundaries, *Comput. Phys. Comm.* 180 (10) (2009) 1811–1820.
- [13] S. Adami, X. Hu, N. Adams, A generalized wall boundary condition for smoothed particle hydrodynamics, *J. Comput. Phys.* 231 (21) (2012) 7057–7075.
- [14] Z. Chen, Z. Zong, M. Liu, L. Zou, H. Li, C. Shu, An SPH model for multiphase flows with complex interfaces and large density differences, *J. Comput. Phys.* 283 (2015) 169–188.
- [15] M. Yildiz, R. Rook, A. Suleman, SPH with the multiple boundary tangent method, *Internat. J. Numer. Methods Engrg.* 77 (10) (2009) 1416–1438.
- [16] W. Dehnen, H. Aly, Improving convergence in smoothed particle hydrodynamics simulations without pairing instability, *Mon. Not. R. Astron. Soc.* 425 (2) (2012) 1068–1082.
- [17] M. Herant, Dirty tricks for SPH, *Mem. Soc. Astron. Ital.* 65 (1994) 1013.
- [18] L.V. Vela, R. Sanchez, J. Geiger, ALARIC: An algorithm for constructing arbitrarily complex initial density distributions with low particle noise for SPH/SPMHD applications, *Comput. Phys. Comm.* (2017).